https://doi.org/10.5194/egusphere-2025-3806
Preprint. Discussion started: 15 August 2025

A 4D-Var Data Assimilation System for the North-Western Mediterranean Sea and its Impact on the Corsica Channel Transport

Michele Bendoni[1], Andrew M. Moore[2], Roberta Sciascia[1], Carlo Brandini[3], Katrin Schroeder[4], Mireno Borghini[1], and Marcello Gatimu Magaldi[1]

[1]CNR-ISMAR, 19032 Lerici (Sp), Italy
[2]Department of Ocean Sciences, University of California, 95062 Santa Cruz CA
[3]CNR-ISMAR, 50019 Sesto Fiorentino (Fi), Italy
[4]CNR-ISMAR, 30122 Venezia (Ve), Italy

Correspondence: Michele Bendoni (michele.bendoni@cnr.it)

Abstract. We present a 4D-Var data assimilation (DA) system covering the North-Western Mediterranean Sea implemented with the Regional Ocean Modeling System (ROMS). We study, throughout the year 2022, its ability to improve the description of the overall circulation and the capability to constrain the transport across the Corsica Channel (CC), the dynamics of which are crucial in determining the circulation throughout the region. The system assimilates Sea Surface Temperature (SST) and Sea Level Anomaly (SLA) observations from satellites, surface velocity data from High-Frequency Radars (HFRs), and in situ temperature, salinity and velocity observations, the latter from a mooring located in the CC. For all the observed state variables, DA is able to improve the forecast and the analysis compared to a free run without DA, with root mean squared error reduction up to 60% and correlation increase up to 0.4. The general circulation after DA is characterized by a reduction of the Eastern Corsica Current (ECC) and an increase of the Western Corsica Current (WCC). An adjoint sensitivity-based method was used to evaluate the impact of observations on the CC transport state estimates. The net reduction in transport induced by DA, changed the annual average value of 0.49 Sv for the free run, to 0.31 Sv and 0.28 Sv for the forecast and analysis, respectively. The observations that contribute most to the transport changes are the in situ velocity data and those from HFRs. The observation impacts were found to vary seasonally, and sometimes act in competition to shape the circulation pathways across the CC. The sensitivity of the transport to SST and in situ temperature and salinity observations indicates that remote measurements (e.g. those from the Gulf of Lion) can potentially play a significant role in constraining the CC transport. Transport variations are largely affected by free surface gradients contained in the increment, and promoted by modifications to the open boundary conditions. This indicates that the CC dynamic is controlled by mechanisms operating at basin scales.

1 Introduction

Data assimilation (DA) is essential for ensuring the quality of both forecasts and reanalysis, in the atmosphere as well as in the ocean. Several ocean models implement 4D-Variational Data Assimilation (4D-Var DA) systems for practical applications

https://doi.org/10.5194/egusphere-2025-3806
Preprint. Discussion started: 15 August 2025

in various regions of the global ocean, where observational coverage is sufficient to meaningfully constrain the circulation estimates.

For example 4D-Var DA system have been implemented at the global scale by the Japan Meteorological Agency (Fujii et al., 2023), and at regional scales in the area between Australia and Indonesia (Janeković et al., 2022), in the coastal waters of eastern Australia (Zavala-Garay et al., 2012; Kerry et al., 2020), in the coastal waters of North America (Zhang et al., 2010; Moore et al., 2013), around several island nations of the Pacific (Arango et al., 2011; Janeković et al., 2013), in the coasts of North Europe (Sperrevik et al., 2015), and in the Mediterranean Sea (Iermano et al., 2016; Janeković et al., 2020; Bendoni et al., 2023).

The north-western Mediterranean Sea (also known ad Liguro-provençal Basin), is a crucial maritime region, hosting the Pelagos Sanctuary (Notarbartolo-di Sciara et al., 2008) and several Marine Protected Areas (MPAs) (Francour et al., 2001). It is characterized by a cyclonic circulation that involves both Atlantic Water (AW) at the surface and Eastern Intermediate Water (EIW) at depth (Astraldi et al., 1994; Schroeder et al., 2024), and by three main circulation branches: the Eastern Corsica Current (ECC) and the Western Corsica Current (WCC), which flow on opposite sides of Corsica and converge to form the Northern Current (NC, or Liguro-Provençal Current, LPC), which flows cyclonically along the Italian coast toward France (Astraldi et al., 1990; Millot, 1999). The ECC passes through the Corsica Channel (CC), a narrow strait between northern Corsica and the Capraia Island, about 30 km wide at the surface and 450 m deep. This strait represents the main connection between the warmer, saltier Tyrrhenian waters and the colder, fresher waters of the Liguro-Provençal basin (Bethoux, 1980; Astraldi et al., 1990). The northward transport across the CC shows a marked seasonal cycle, with higher values during winter and spring and a net reduction in summer and autumn (Astraldi and Gasparini, 1992), occasionally reversing direction (Sciascia et al., 2019). The CC significantly influences Mediterranean dynamics by affecting the Ligurian Current and the Mediterranean Deep Water formation process (Schroeder et al., 2010), shaping biological connectivity between the Tyrrhenian and Ligurian Seas depending on flow strength (Astraldi et al., 1995), and playing a key role in the accumulation and dispersal of floating debris and pollutants (Fossi et al., 2017), making it a critical area for understanding oceanographic, ecological, and environmental processes in the region.

Several DA systems have been implemented at the basin scale in the Mediterranean Sea, targeting both physical (Dobricic et al., 2005; Escudier et al., 2021; Bajo et al., 2023), and biogeochemical variables (Teruzzi et al., 2018). Regional DA applications in the western basin differ by algorithm (e.g., variational methods, ensemble-based Kalman filters) and by scientific objectives. Particular attention has been paid to the assimilation of surface velocities from High-Frequency Radars (HFRs), either alone or in combination with standard observations such as sea surface temperature (SST), sea level anomaly (SLA), and in situ temperature and salinity. Marmain et al. (2014) used observations to adjust atmospheric forcing off the French coast in front of Toulon, while Vandenbulcke et al. (2017) aimed to correct the inertial oscillation in the Ligurian Sea. Iermano et al. (2016) and Bendoni et al. (2023) both applied 4D-Var to improve circulation estimates in the Tyrrhenian and north-western Mediterranean, respectively, analyzing the effect of different observation types on alongshore coastal transport. Hernandez-Lasheras et al. (2021) used HFR data to better resolve mesoscale dynamics in the westernmost part of the Mediterranean basin, while Hernandez-Lasheras and Mourre (2018) compared model results after assimilating glider and CTD (conductivity-temperature-

https://doi.org/10.5194/egusphere-2025-3806
Preprint. Discussion started: 15 August 2025

depth) data. Aydogdu et al. (2025) examined the impact of the assimilation of autonomous glider data by comparing outputs from three different models with partially overlapping domains.

Despite numerous modeling studies, both with (Vandenbulcke et al., 2017; Escudier et al., 2021) and without DA (Béranger et al., 2005; Sciascia et al., 2019; Poulain et al., 2020), and although the CC is included in their domains, a detailed assessment of how assimilation improves the current representation in the channel is still lacking. Furthermore, starting from the theoretical basis and the numerical algorithms employed to calculate the increment, DA systems offer tools to analyze several aspects of the assimilation procedure. For example, observation impact experiments allow evaluation of how different data sources affect scalar quantities such as net volume and energy transport across a section, or upwelling intensity (Moore et al., 2011a; Levin et al., 2020, 2021). Quantifying the contribution of different observations to transport increments through the CC can thus provide insight into the dominant dynamical scales.

In this paper, we present an improved version of the 4D-Var DA system previously implemented by Bendoni et al. (2023) for the north-western Mediterranean, using the ROMS model (Shchepetkin and McWilliams, 2003, 2005). In addition to HFR-derived surface velocities and satellite SST, the system also assimilates SLA, in situ temperature, salinity and current profiles for the year 2022. The DA configuration and the observation impact methodology are described in Section 2. The performance of the system in improving circulation with respect to a non-assimilative model run is assessed in Section 3, with a focus on the agreement with observations. The impact of assimilated observations on the Corsica Channel volume transport is also evaluated in Section 3, together with a discussion on the main findings. Section 4 concludes the paper with final remarks and outlooks.

2 ROMS 4D-Var DA system for the NWM

2.1 Model setup

The ROMS 4D-Var Data Assimilation system (Moore et al., 2011b) implemented for this study (Figure 1), builds upon the configuration developed by Bendoni et al. (2023), with some modifications applied to both the nonlinear model and the data assimilation framework. Specifically, the same numerical grid (1/36° resolution with 40 terrain-following sigma layers) is used and the following model parameters are adopted: $V_{transform} = 2$, $V_{stretching} = 4$, $\theta_s = 7$, $\theta_b = 2$, $\nu = 5$ [m^2/s], $\kappa_T = 1$ [m^2/s]. The k-kl GLS (Generic Length Scale) scheme for turbulence closure parameters is adopted (Warner et al., 2005).

Initial and boundary conditions are derived from the Mediterranean Sea Physics Reanalysis (Escudier et al., 2021) provided by the Copernicus Marine Environment Monitoring Service (CMEMS), at 1/24° resolution and daily frequency. These are imposed at the southern open boundary. Radiation boundary conditions are applied at all depths to velocity components (u, v), temperature (T) and salinity(S), with a one-day nudging timescale for inflow points and a threefold increase for outflow conditions (Marchesiello et al., 2001). A Flather condition (Flather, 1976) is used for barotropic velocities, a Chapman condition (Chapman, 1985) for the free surface η, and a zero gradient condition for total kinetic energy (TKE). Atmospheric forcing is provided at hourly frequency from the ERA5 reanalysis dataset (Hersbach et al., 2023), including sea-level pressure, 10-m air temperature and relative humidity, precipitation rate, surface wind components, and downward short- and long-wave radiations.

https://doi.org/10.5194/egusphere-2025-3806
Preprint. Discussion started: 15 August 2025

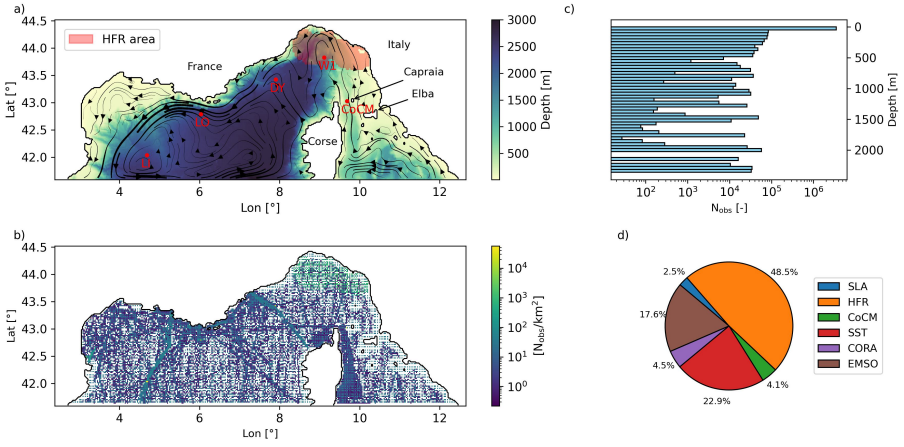

Figure 1. a) Model domain with yearly averaged surface current for the free-run without assimilation, superimposed to model bathymetry. Red dots represent the mooring stations from EMSO (LI: Lion, LO: Albatross, DY: Dyfamed, W1: W1M3A) and JERICO (CoCM: Corsica Channel Mooring). Red shaded area represents the extend of the JERICO HF radar network. b) Spatial horizontal density of the assimilated observations. c) Vertical distribution with depth of the assimilated observations. d) Proportion of the different sources of observations with respect to the total.

These variables are used to compute air-sea fluxes following the bulk formulation of Fairall et al. (1996). Daily river discharge data for the Rhone and Arno rivers were obtained from the Hydro Portal of France Waters (https://www.hydro.eaufrance.fr), and the Tuscany Region SIR Dataset (https://www.sir.toscana.it), respectively. The nonlinear model without assimilation was run from 2019 to 2022, after a three-month spin-up starting in late 2018. The DA experiment spans the period January-December 2022, starting from an initial first-guess provided by the free nonlinear model run on 1 January 2022 at 00:00.

The ROMS state vector comprising all ocean gridpoint values of temperature, salinity, horizontal velocity and free surface height will be denoted by $\mathbf{x}$. The analysis state vector $\mathbf{x}_a$ in 4D-Var DA can then be expressed by the following equation:

$$\mathbf{x}_a = \mathbf{x}_b + \mathbf{B}\mathbf{G}^T(\mathbf{G}\mathbf{B}\mathbf{G}^T + \mathbf{R})^{-1}\mathbf{d} = \mathbf{x}_b + \mathbf{K}\mathbf{d} \tag{1}$$

where $\mathbf{K}$ is the so called Kalman gain matrix, $\mathbf{x}_b$ is the background state vector, $\mathbf{B}$ is the background error covariance matrix (incorporating background errors associated to initial and boundary conditions and atmospheric forcing), $\mathbf{G}$ is the tangent linear model sampled at observation locations and $\mathbf{G}^T$ its adjoint. $\mathbf{R}$ is the observation error covariance matrix, and $\mathbf{d} = \mathbf{y} - H(\mathbf{x}_b)$ is the innovation vector, with $\mathbf{y}$ the observation vector, and H the observation operator, which maps from the state space to the observation space and includes the nonlinear model in 4D-Var DA. The matrix $\mathbf{P} = \mathbf{G}\mathbf{B}\mathbf{G}^T + \mathbf{R}$ is the stabilized representer matrix describing the total error covariance in observation space (Moore et al., 2018, 2021).

In practice, the analysis is obtained by minimizing a cost function following the incremental approach of Courtier et al. (1994), as implemented in ROMS by Moore et al. (2011b). Sequential linearizations of the cost function around a nonlinear solution (an "outer loop") similar to a Gauss-Newton method, give rise to a series of quadratic problems which are minimized using the Lanczos formulation of the Restricted $\mathbf{B}$-Preconditioned Conjugate Gradient algorithm (RPCG), implemented as

https://doi.org/10.5194/egusphere-2025-3806
Preprint. Discussion started: 15 August 2025

a sequence of "inner loops", as described by Gürol et al. (2014). The algorithm factorizes the $\mathbf{R}$-preconditioned stabilized representer matrix $\tilde{\mathbf{P}} = \mathbf{R}^{-1}\mathbf{G}\mathbf{B}\mathbf{G}^T + \mathbf{I}$, yielding an approximation of the Kalman gain matrix of the form:

$$\mathbf{K} \approx \mathbf{B}\mathbf{G}^T\mathbf{V}_m\mathbf{T}_m^{-1}\mathbf{V}_m^T\mathbf{G}\mathbf{B}\mathbf{G}^T\mathbf{R}^{-1} \tag{2}$$

where $\mathbf{V}_m$ is the matrix of Lanczos vectors, $\mathbf{T}_m$ is a tridiagonal matrix, and m is the number of inner loops.

In this study, we use a single outer loop and 9 inner loops. The assimilation window is 3 days long, resulting in 122 windows over the year 2022. The choice of 2022 is motivated by the broader availability of HFR observations during this year. Each analysis (AN) uses the forecast (FC) from the previous window as background; hence, in the following, the terms "forecast" and "background" are used interchangeably. A strong constraint approach is adopted, where the control vector includes the initial conditions, open boundary conditions, and surface fluxes, but no model error is explicitly considered (Moore et al., 2011b).

The background error covariance matrix is modeled following Weaver and Courtier (2001). Climatological variances of model state variables, computed from the free run over 2019-2022, are used as proxies for background error variances. To remove diurnal and seasonal signals, temperature and heat flux time series were detrended using a moving average with quarterly and daily timescales. The background error covariance matrix is factorized as $\mathbf{B} = \mathbf{\Sigma}\mathbf{C}\mathbf{\Sigma}$ where $\mathbf{\Sigma}$ is a diagonal matrix of standard deviations, and $\mathbf{C}$ a univariate correlation matrix with a specified decorrelation length, modeled with a diffusion operator. Horizontal and vertical decorrelation length scales were set to 15 km and 10 m, respectively, for all state variables associated with initial and boundary conditions, and to 70 km for surface fluxes. Although $\mathbf{B}$ is assumed univariate, flow-dependent cross-covariances emerge during the assimilation window via $\mathbf{G}\mathbf{B}\mathbf{G}^T$ in Equation 1. For practical reasons, the observation error covariance matrix $\mathbf{R}$ is considered diagonal. Error values for each observation type are discussed in section 2.2).

2.2 Assimilated observations

Several observational datasets were assimilated into the model, including surface currents from the Tyrrenian-Ligurian HFR network, in situ velocities, temperature and salinity measurements from various platforms, and satelite-derived SST and SLA.

HFR total surface currents u and v from the European HFR Node (https://www.hfrnode.eu) cover parts of the Ligurian Sea (Figure 1a) being JERICO (Joint panEuropean Research Infrastructure for Coastal Observatories, https://www.jerico-ri.eu) facilities. These data are provided at 2.0 km resolution and hourly frequency for 2022. Before assimilation, a 3-hour low-pass filter was applied at each location to the u and v time series to remove high-frequency variability. Only observations flagged as "good" with a geometric dilution of precision (GDOP) larger than 2 were retained (Fang et al., 2015). Furthermore, at each time step, outliers-defined as velocities above the 99.5%-ile-were excluded. To reduce the HFR data volume and redundancy (Figure 1d), the u and v velocities were averaged into 6 km bins and sub-sampled every 3 hours. Visual inspection confirmed that the spatially averaged fields retained key patterns. Despite this thinning, HFR data still comprised nearly half of all assimilated observations (Figure 1d). The HFR observation error standard deviation was set to 0.1 m/s Hernandez-Lasheras et al. (2021); Bendoni et al. (2023).

https://doi.org/10.5194/egusphere-2025-3806
Preprint. Discussion started: 15 August 2025

In situ velocities were also obtained from the Corsica Channel Mooring (CoCM, Figure 1a) (Aracri et al., 2016), which is also a JERICO facility and includes an upward-facing acoustic doppler current profiler (ADCP) deployed at 450 m depth. The instrument recorded data at 16 m vertical intervals (from 379 m upward) every 2 hours. Observations with a multibeam-derived "indicative error" (GLGOPV) outside the $[-0.1, 0.1]$ m/s range-mostly from depths shallower than 50 m-were excluded due to unrealistic signal shifts. A 6-hour moving average was applied to the time series before assimilation, and the observation error standard deviation was set to 0.05 m/s.

In situ temperature and salinity data were obtained from CMEMS and the European Multidisciplinary Seafloor and water column Observatory (EMSO-ERIC https://emso.eu). CMEMS data (product INSITU_GLO_PHY_TS_DISCRETE_MY_013_001, Szekely et al. (2025)) include time series and profile datasets (Tac, 2023). They are part of the Global Ocean CORA In situ Observations, and we refer to them as T_{CORA} and S_{CORA} to indicate temperature and salinity data, respectively, without making the same distinction unless otherwise noted. Only data with all quality flags equal to "good" were used. EMSO data are temperature (T_{EMSO}) and salinity (S_{EMSO}) time series from four different mooring platforms: Lion (LI) in the Gulf of Lion (https://www.seanoe.org/data/00333/44411, Houpert et al. (2016)), Albatross (LO) near Toulon (https://www.seanoe.org/data/00720/83244, Lefevre et al. (2016)), Dyfamed (DY) in the western Ligurian Sea (https://www.seanoe.org/data/00326/43749, Coppola et al. (2019)), and W1M3A (W1) in the central Ligurian Sea (www.w1m3a.cnr.it). Locations are reported in Figure 1a. Observation error standard deviations were set to 0.2°C for temperature and 0.075 for salinity. Satellite-derived SST was obtained from the CMEMS Mediterranean Sea High Resolution L3S Sea Surface Temperature product (SST_MED_SST_L3S_NRT_OBSERVATIONS_010_012) with a spatial resolution of 1/16° (Buongiorno-Nardelli et al., 2013). The assigned observation error standard deviation was 0.4° C. Along track SLA data were sourced from the CMEMS SEALEVEL_EUR_PHY_L3_MY_008_061 product, which includes data from multiple altimeter missions (Cryosat-2, HY-2B, Jason-3, Saral/Altika, Sentinel-3A, Sentinel-3B, and Sentinel-6A) at 7 km resolution. The assimilated quantity was the absolute dynamic topography (ADT), computed as a sum of the SLA and the mean dynamic topography (MDT). A bias correction was applied by subtracting the temporal mean of ADT and adding the MDT from the 2019-2022 ROMS free run, interpolated along the satellite tracks. To better constrain the free surface, each SLA observation was repeated one hour before and after its timestamp, following the assumption of slowly varying sea level signals Zavala-Garay et al. (2014) and Levin et al. (2021). Super-observations were created by averaging data within the same model grid cell (horizontally and vertically) and time window (hourly), as described by (Moore et al., 2011b). A background quality control procedure was applied following (Moore et al., 2013), rejecting observations when $d_i^2 > \beta^2(\sigma_{\text{b}}^2 + \sigma_{\text{o}}^2)$, where d_i is the i-th component of the innovation, σ_{b}^2 is the background error at observation location, σ_{o}^2 is the observation error variance and β is a coefficient that depends on the type of observation. Here β was assigned a value 5 for all observation types meaning that observations with innovations that exceed five times the square root of the expected total error variance are rejected.

The spatial density of assimilated observations is reported in Figure 1b, while the distribution with depth and typology is reported in Figures 1c and 1d, respectively. In total, approximately $4.5 \cdot 10^6$ observations were assimilated during 2022, with a mean of $36.4 \cdot 10^3$ observations per assimilation cycle. Further temporal and depth-dependent distributions by data source are presented in Figures 3 and 4.

https://doi.org/10.5194/egusphere-2025-3806
Preprint. Discussion started: 15 August 2025

2.3 Quantifying impact of observations

The properties of the adjoint model allow quantification of the impact that each assimilated observation has on a specific scalar metric $I(\mathbf{x})$, following the approach described by Langland and Baker (2004). Specifically, the increment in the metric $\Delta I(\mathbf{x}) = I(\mathbf{x}_a) - I(\mathbf{x}_b)$ due to DA (Moore et al., 2011a, 2017) can be approximated as:

$$\Delta I(\mathbf{x}) \approx \mathbf{d}^T \mathbf{K}^T \mathbf{M}_\mathbf{b}^T(t) \partial I / \partial \mathbf{x} \tag{3}$$

where $\mathbf{M_b}(t)$ is the tangent linear model computed around the background state $\mathbf{x}_b$. In this study, we consider the time-averaged volume transport integrated over a transect, expressed as: $I(\mathbf{x}) = \frac{1}{N_t}\sum_{n=1}^{N_t} \mathbf{h}_n^T \mathbf{v}_{\perp,n} = \overline{Tr}$ where N_t is the total number of time steps, $\mathbf{v}_{\perp,n}$ is the velocity component orthogonal to the transect, and $\mathbf{h}_n$ is a vector comprising the contributions to cross-sectional area at each time step n. After replacing $\mathbf{K}$ by the approximation in equation 2, the impact $\Delta I(\mathbf{x})$ on transport becomes:

$$\Delta I(\mathbf{x}) \approx \frac{1}{N} \mathbf{d}^T \mathbf{R}^{-1} \mathbf{G} \mathbf{B} \mathbf{G}^T \mathbf{V}_m \mathbf{T}_m^{-1} \mathbf{V}_m^T \mathbf{G} \mathbf{B} \sum_{n=1}^{N_t} \mathbf{M}_\mathbf{b}^T(t_n) \mathbf{h}_n \tag{4}$$

The contribution of a single observation y_i is readily computed from the dot-product of the i-th component of the innovation $\mathbf{d}$ and the i-th component of the vector $\mathbf{g} = \mathbf{K}^T \mathbf{M}_\mathbf{b}^T(t) \partial I / \partial \mathbf{x}$. Therefore, the averaged increment for an assimilation window is $\Delta I(\mathbf{x}) = \sum_{i=1}^{N_{\text{obs}}} d_i \cdot g_i = \Delta \overline{Tr}$. Moreover, the total observation impact can be decomposed according to the control vector to the 4D-Var increments as $\Delta I(\mathbf{x}) = \mathbf{d}^T \cdot (\mathbf{g_x} + \mathbf{g_f} + \mathbf{g_b}) = \sum_{i=1}^{N_{\text{obs}}} d_i \cdot (g_{x,i} + g_{f,i} + g_{b,i})$ where $\mathbf{g_x}$, $\mathbf{g_f}$ and $\mathbf{g_b}$ represent the contributions to $\mathbf{g}$ from the initial conditions, surface forcing and open boundary conditions, respectively (Moore et al., 2011a).

In the present work, we focus on the volume transport across the Corsica Channel, evaluated along a transect between (9.4250E, 43.0204N) and (9.8369E, 43.0204N). We quantify the contribution of the different observation platforms to the resulting transport increments and their respective influence on each component of the 4D-Var control vector.

3 Results and Discussion

3.1 Performance of the DA System

A first indication of the effectiveness of the assimilation procedure in fitting the model to observations is provided by the behavior of the cost function J. Figure 2a shows the initial and final values of J, along with the ratio of the final to initial observation-related cost component, $J_\text{o} = \frac{1}{2}[\mathbf{y} - H(\mathbf{x})]^T \mathbf{R}^{-1} [\mathbf{y} - H(\mathbf{x})]$. Final values of J are consistently lower than the initial ones, with the ratio $J_{\text{o,fin}}/J_{\text{o,ini}}$ ranging between 0.2 and 0.6.

Insight into potential overfitting to the observations is provided by analyzing the eigenvalues of the $\mathbf{R}$-preconditioned stabilized representer matrix $\tilde{\mathbf{P}}$ (McIntosh and Bennett, 1984; Moore et al., 2018, 2021). The majority of the increment $\delta\mathbf{x}$ is typically associated with the smallest eigenvalues, which may introduce spurious noise and degrade the solution. Therefore, a useful rule-of-thumb to prevent overfitting is to retain only the contributions from eigenvalues λ_i satisfying $\lambda_i/\lambda_{\max} > 0.01$

https://doi.org/10.5194/egusphere-2025-3806
Preprint. Discussion started: 15 August 2025

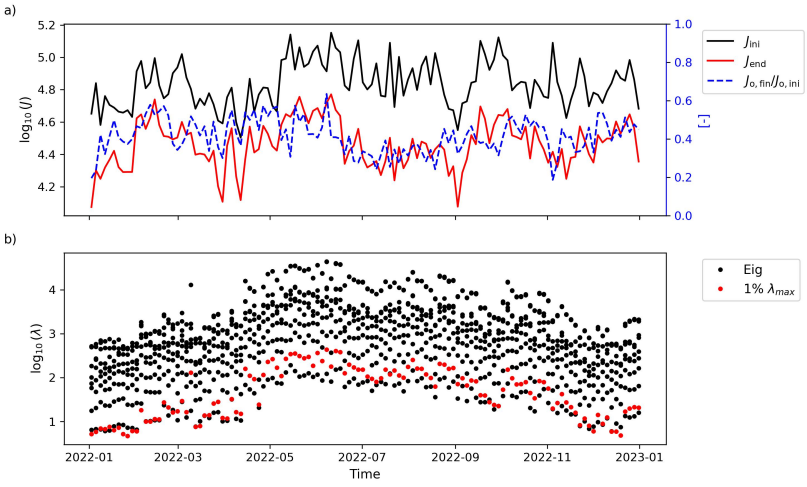

Figure 2. a) Temporal behavior of the initial cost function (black line), its value after data assimilation (red line), and the ratio of the final to the initial value of the part of the cost function related to observations (blue dashed line). b) Eigenvalues of the matrix $\mathbf{T}_m$ (black dots) and 1% values of the largest eigenvalue (red dots), for each assimilation window.

(McIntosh and Bennett, 1984). Since the eigenvalues of $\tilde{\mathbf{P}}$ match those of the tridiagonal matrix $\mathbf{T}_m$, they can be directly computed as a diagnostic during each 4D-Var cycle. Figure 2b shows that the number of inner loops used does not lead to significant overfitting, with at most only the final eigenvalue falling below the $0.01\lambda_{\max}$ threshold.

Model performance in reproducing observations is shown in Figure 3 and Figure 4 for the FR, FC and AN runs. Figure 3 shows the time evolution of the root mean square error (RMSE), computed over individual assimilation windows, for spatially distributed variables: surface velocities from HFR, u_{HFR} and v_{HFR}, CORA in situ temperature and salinity T_{CORA} and S_{CORA}, and satellite-derived SST and SLA. RMSE is calculated as $\frac{1}{N^{\mathrm{w}}_{\mathrm{obs}}}\sum_{i=1}^{N^{\mathrm{w}}_{\mathrm{obs}}}\sqrt{y_i - y_i^{\mathrm{m}}}$, where $N^{\mathrm{w}}_{\mathrm{obs}}$ is the number of observations for a specific observed variable during an assimilation window, y_i is the i-th observation value and $y_i^{\mathrm{m}} = H(x)$ the model counterpart in observation space. The number of observations per window is also shown as a gray bar on the secondary y axis. The assimilation improves both FC and AN runs with respect to the FR across all variables (Figure 3 g). For surface currents measured by the HFR, a difference between the three runs, with the FC falling between FR and AN is clearly observable (Figure 3a and b). The weighted average RMSE reduction compared to FR is between 10.1% (u) and 17.7% (v) for the forecast ($\overline{\Delta\mathrm{RMSE}^*}_{\mathrm{FC}}$) and between 33.7% ($u$) and 40.8% ($v$) for the analysis ($\overline{\Delta\mathrm{RMSE}^*}_{\mathrm{AN}}$) (Table 1). CORA in-situ observations of T and S (Figure 3c and d) exhibit periods where FC and AN are similar-especially for salinity-(Figure 3d) and with a quite large variability in the number of observations, which decreases in the second half of the year. The RMSE reduction for FC and AN in temperature, $\overline{\Delta\mathrm{RMSE}^*}_{\mathrm{FC}}$ and $\overline{\Delta\mathrm{RMSE}^*}_{\mathrm{AN}}$ for T_{CORA} are equal to -25.6% and -46.7%, respectively. A similar result holds for S_{CORA} (Table 1). SST shows a notable RMSE increase for the FR, and less so for the FC, starting in May, while $\mathrm{RMSE}_{\mathrm{AN}}$ tends to remain more stable (Figure 3e). Reduction in error ranges from 21.2 to 52.5 % for FC and AN, respectively (Table 1). For the SLA the improvement due to the DA procedure is evident throughout the year for the AN, whereas for the FC it is

https://doi.org/10.5194/egusphere-2025-3806
Preprint. Discussion started: 15 August 2025

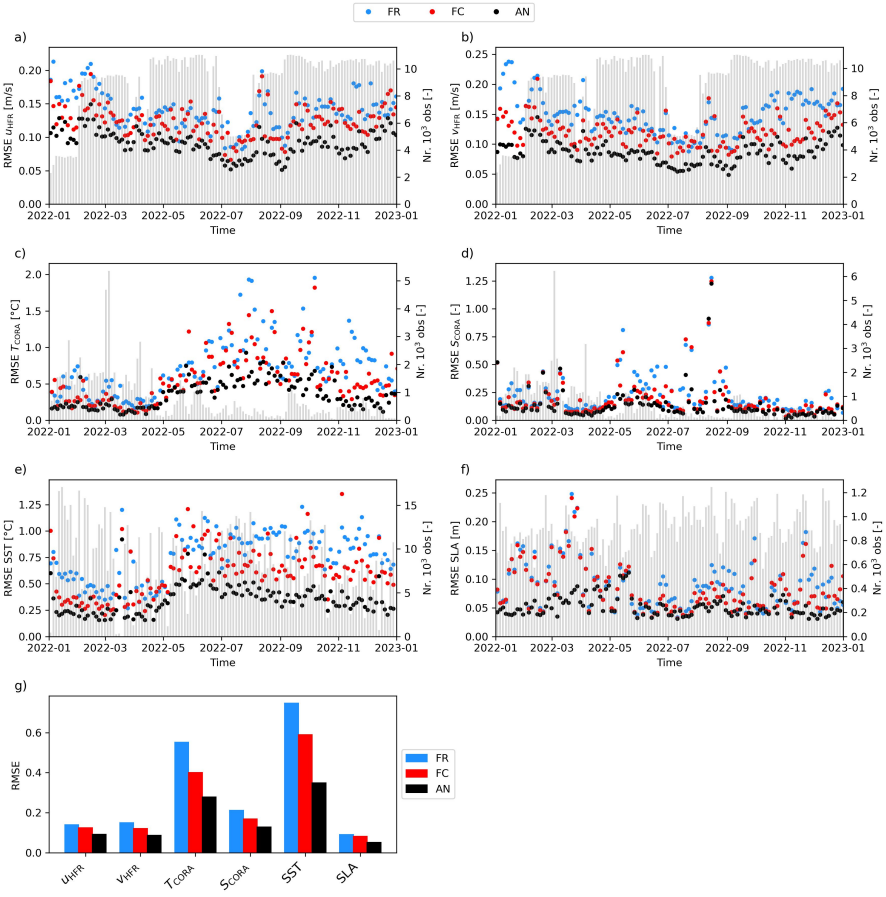

Figure 3. Time series of the RMSE between modeled and observed values for the free run (FR) in blue, forecast (FC) in red and analysis (AN) in black. Grey bars represent the amount of assimilated observations during each assimilation window .a) and b) u- and v-velocity components from HFR, respectively; c) and d) in situ temperature and salinity from the CORA dataset, respectively; e) SST, f) SLA. In g) the average RMSE weighted on the number of observation per assimilation window for the variables analyzed is reported.

more pronounced from the second half of June (Figure 3f). Indeed, the error reduction is 8.3 % for the forecast and 33.6% for the analysis (Table 1).

For observations collected by fixed platforms (those from the JERICO CoCM and the EMSO platforms), the vertical distribution of RMSE is shown in Figure 4 (panels a to d). Also in this case, the data assimilation procedure leads to a general improvement in the model skills for both the AN and FC fields across all observed variables (Figure 4e). For the current velocities observed by the JERICO CoCM mooring, the RMSE reduction is more pronounced for the meridional (v) component than for the zonal (u) component, with the v velocity reaching a maximum $\overline{\Delta \mathrm{RMSE}^*}_{\mathrm{AN}}$ of -62.4 % (Table 1 and Figure 4a and b). In situ temperature and salinity observations from the EMSO platforms show an uneven vertical distribution (Figure 4c and d), and a variable number of observations across platforms (Figure 4f). The RMSE reduction for both FC and AN is more

https://doi.org/10.5194/egusphere-2025-3806
Preprint. Discussion started: 15 August 2025

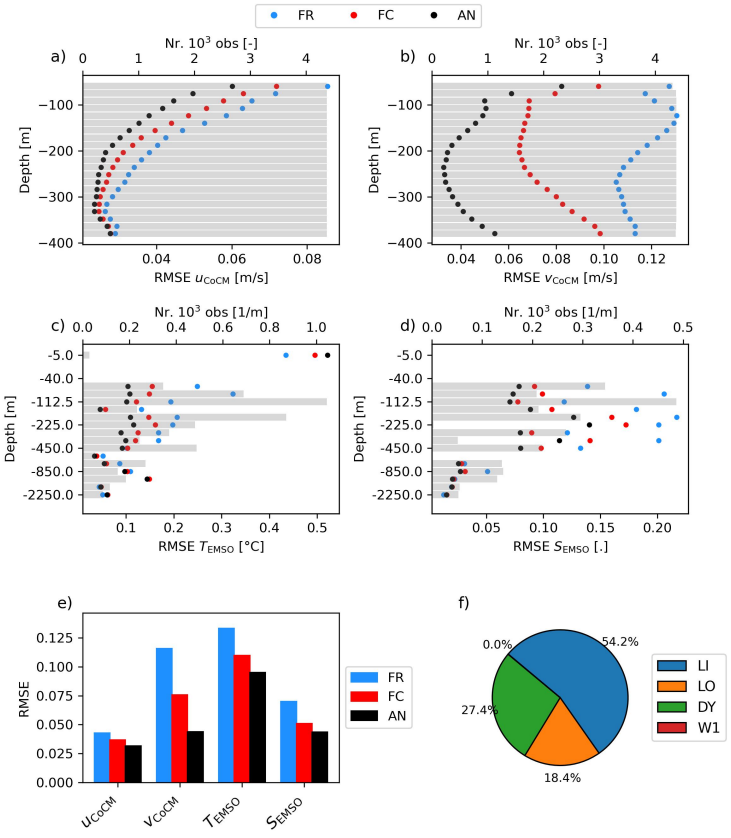

Figure 4. Distribution with depth of the RMSE between modeled and observed values for the free run (FR) in blue, forecast (FC) in red and analysis (AN) in black. Grey bars represent the number of assimilated observations at each depth; a) and b) u- and v-velocity components from the JERICO CoCM, respectively; c) and d) in situ temperature and salinity from the EMSO dataset, respectively. e) Average RMSE weighted on the number of observation per assimilation window for the variables analyzed is reported. f) Quantitative distribution of observations per platform (Figure 1).

evident above 450 m depth, while differences between the three simulations become less significant below this depth, down to 2250 m (Figure 4c and d). The $\overline{\Delta\text{RMSE}^*}$ is larger for the S_{EMSO} than for the T_{EMSO} (Table 1).

The improvement obtained through DA was also evaluated using the Pearson's correlation coefficient, $\rho = \frac{\sum_{i=1}^{N_{\text{obs}}^{\text{w}}} [y_i - \text{avg}(\mathbf{y})][y_i^{\text{m}} - \text{avg}(\mathbf{y}^{\text{m}})]}{\text{std}(\mathbf{y}) \cdot \text{std}(\mathbf{y}^{\text{m}})}$, and the global mean difference (BIAS). The change in global BIAS ($\overline{\Delta\text{BIAS}}$) and in mean correlation ($\overline{\Delta\rho}$) between the different model runs are reported in Table 1, further confirming the overall positive impact of data assimilation on model performance.

The correlation between model output and observations consistently increases following the DA procedure, as indicated by positive values of $\overline{\Delta\rho}$ (Table 1). In contrast, the global BIAS shows a slight increase in some cases relative to the FR. However, BIAS values remain generally smaller than the standard deviation of the observed variables, regardless of wether

https://doi.org/10.5194/egusphere-2025-3806
Preprint. Discussion started: 15 August 2025

Variable	$\overline{\Delta\text{RMSE}^*}$ [%]		$\overline{\Delta\rho}$ [-]		$\overline{\Delta\text{BIAS}}$ [m.u.]	
	FC	**AN**	**FC**	**AN**	**FC**	**AN**
u_{HFR}	-10.1	-33.7	0.14	0.38	0.005	-0.002
v_{HFR}	-17.7	-40.8	0.20	0.38	0.013	-0.026
u_{CoCM}	-13.3	-23.6	0.21	0.36	0.004	0.003
v_{CoCM}	-34.1	-62.4	0.15	0.38	-0.072	-0.078
T_{CORA}	-25.6	-46.7	0.02	0.04	-0.094	-0.109
S_{CORA}	-19.2	-39.4	0.07	0.20	-0.023	-0.030
T_{EMSO}	-10.1	-18.7	0.16	0.21	-0.036	-0.034
S_{EMSO}	-15.2	-22.4	0.31	0.41	-0.021	-0.028
SST	-21.2	-52.5	0.06	0.17	-0.071	-0.094
SLA	-8.3	-35.6	0.04	0.08	0.015	0.001

Table 1. Columns 2 and 3 show the average relative difference of RMSE between the forecast and freerun (FC), and the analysis and freerun (AN), weighted on the number of observation for each assimilation window for each observation type in column 1; negative values indicate improvement and vice-versa. Columns 4 and 5 show the average increase/decrease in Pearson's ρ correlation between forecast and freerun (FC), and analysis and freerun (AN), weighted on the number of observation for each assimilation window; positive values indicate improvement and vice-versa. Columns 6 and 7 show the difference in the mean total bias (in absolute value) between forecast and freerun (FC), and analysis and freerun (AN). For the $\overline{\Delta\text{BIAS}}$ each value have the measurement unit of the associated variable; negative values indicates improvement and vice-versa.

model performance improves or slightly deteriorates. For instance, the increase in $\overline{\Delta\text{BIAS}}$ for u_{CoCM} ranges between 0.003 and 0.004 m/s, compare to the standard deviation of 0.037 m/s in the observations. Similarly, for SLA, $\overline{\Delta\text{BIAS}}$ varies between 0.001 and 0.015 m, while the standard deviation of the observed SLA is 0.053 m.

Regarding the circulation, Figure 5 presents time- and depth-averaged currents from FR and AN over two vertical layers: surface to 200 m (AW), and 250-450 m (EIW) (Artale and Gasparini, 1990).

DA slightly intensifies the NC, primarily by strengthening the WCC, which is barely noticeable in the FR, while the ECC flow is reduced (Figure 5a and b). This pattern aligns with previous studies showing higher ECC variability and average speed (Astraldi et al., 1990; Astraldi and Gasparini, 1992), though comparison is complicated by the position of the mooring used to measure WCC, north of Corsica, east of the dominant streamlines, and near the junction between the WCC and ECC. A similarly pronounced WCC signal was also reported by Ciuffardi et al. (2016). In the HFR domain, DA deflects the flow more westward, softening the curvature observed in FR. Cyclonic structures between 4° and 8°E, weakly defined in FR, are more marked in AN. Similar differences are seen in the EIW layer (Figure 5c and d).

Figure 6 compares the observed and modeled northward velocity component of the JERICO CoCM time series at three different depths to evaluate DA performance in reproducing transport through the Corsica Channel. Figure 6a-c shows better agreement in AN than FR. Winter velocity peaks are generally captured, albeit the FR shows surface overestimation and bottom underestimation in late 2022. Annual mean profiles of northward velocity across the channel (Figure 6d, e) confirm

https://doi.org/10.5194/egusphere-2025-3806
Preprint. Discussion started: 15 August 2025

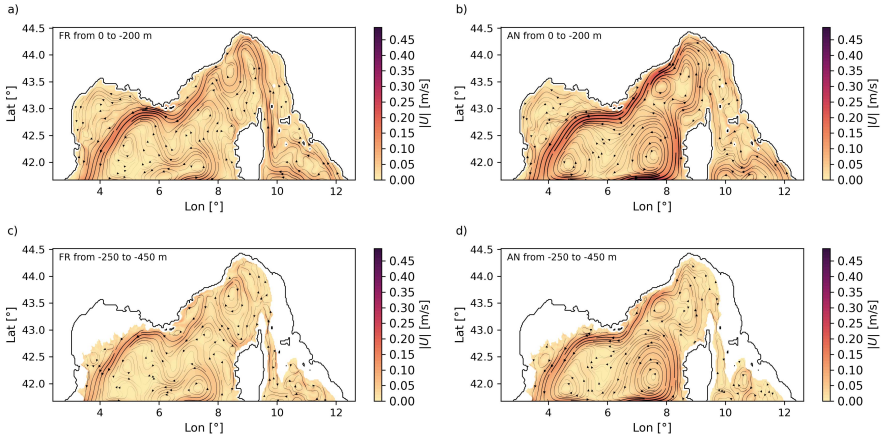

Figure 5. Depth and yearly averaged currents for different depth ranges as streamlines superimposed to the velocity magnitude $|U|$. a) freerun for the depth interval from the surface to -200; b) analysis for the depth interval from the surface to -200 m; d) freerun for the depth interval from -250 m to -450 m; e) analysis for the depth interval from -250 m to -450 m.

these trends: FR overestimates velocity, while AN aligns well with observations. Negative velocity areas are reduced in AN. Differences between AN and FC are minor and are not shown.

3.2 Observation Impact on Corsica Channel Transport

A useful metric for assessing the effectiveness of the DA procedure is the scatter plot of the contribution of each observation (i.e., its impact on δI) versus the innovation ($\mathbf{d}$), as illustrated in Figure 7. These scatter plots can also be interpreted as contingency diagrams, with the percentage of points in each quadrant indicated. Overall, the points in Figure 7 are approximately evenly distributed between positive and negative innovations for all observation types, suggesting that there is no significant bias in these observed components of the state vector. The "butterfly" shape of each scatter plot indicates that observations with small innovations tend to produce only minor changes in CC transport. This behaviour is expected, as observations that require only small corrections on the background state should not significantly alter transport estimate. Conversely, observations associated with larger innovations, exhibit a wider range of impacts on CC transport. By and large, for HFR, SST, SLA, CoCM and in situ salinity, impacts are approximately symmetrically distributed around $\delta I = 0$, meaning that these data sources contribute both positively and negatively to CC transport adjustments. In contrast, in situ temperature observations show a skewed distribution, with approximately 61% of the points leading to a reduction in transport ($\delta I < 0$). Figure 7 also reveals a pronounced asymmetry in the distribution of points relative to $d_i = 0$ for SLA and CoCM observations. Specifically, negative SLA innovations ($d_i < 0$) typically lead to an increase in CC transport ($\delta I < 0$), and vice versa. The opposite pattern is observed for CoCM data. While such a behavior is clear for the CoCM v-velocity component, further analysis is needed to fully understand the underlying mechanism driving the SLA signal in the DA system.

https://doi.org/10.5194/egusphere-2025-3806
Preprint. Discussion started: 15 August 2025

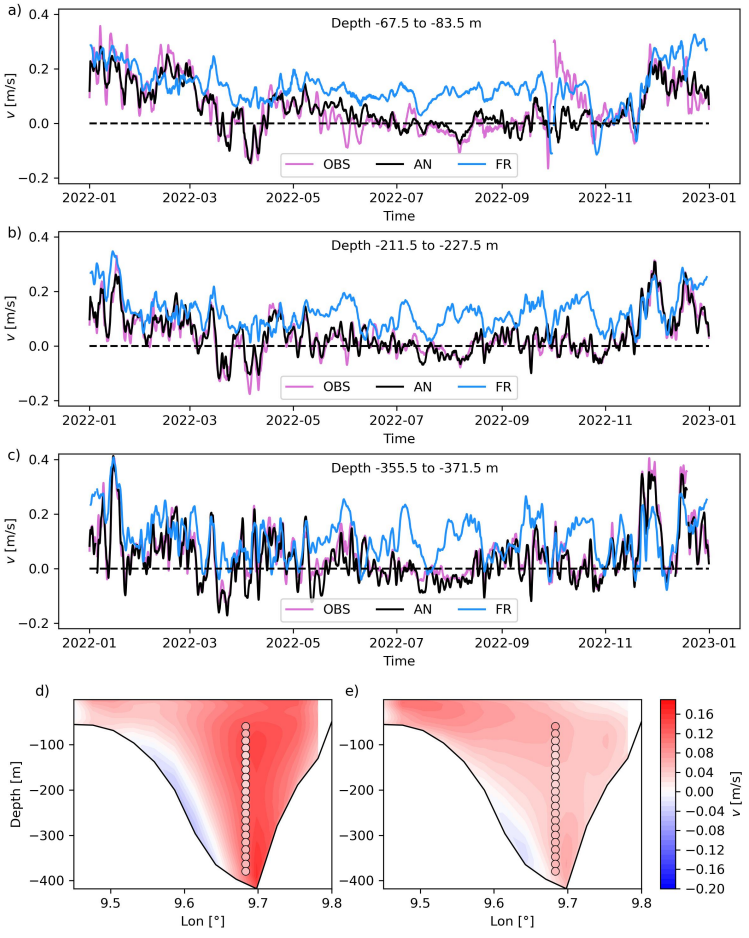

Figure 6. Time evolution of the observed (violet), and modeled by FR (light blue) and AN (black) runs of the v-component of the velocity at the JERICO CoCM at different depth intervals: a) from -67.5 to -83.5; b) from -211.5 to 227.5; c) from -355.5 to -371.5). Yearly averaged value of the v-component of the velocity at the transect in correspondence of the CC mooring for FR d) and AN e), together with yearly averaged observed values (colored dots).

https://doi.org/10.5194/egusphere-2025-3806
Preprint. Discussion started: 15 August 2025

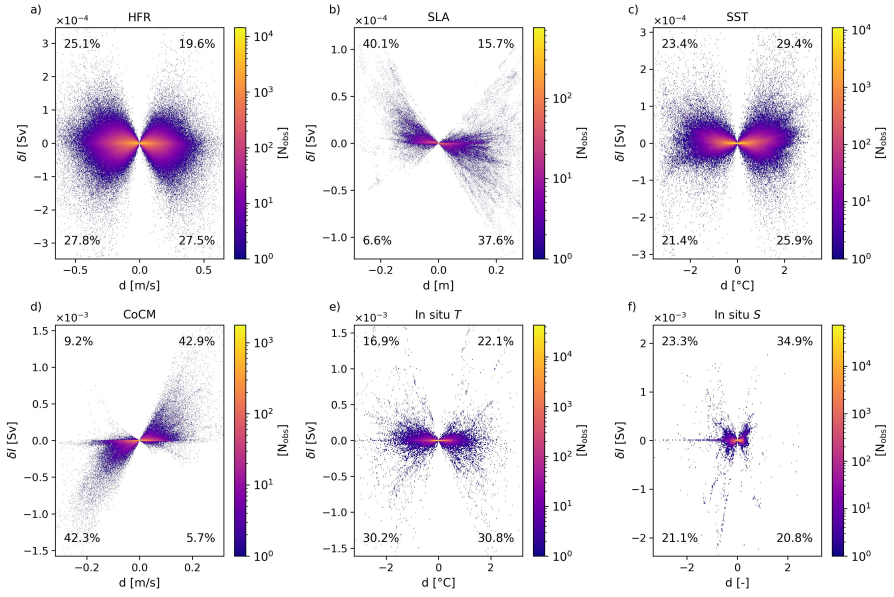

Figure 7. Density scatter plot of innovation $\mathbf{d}$ versus increment δI for different typology of observations: a) high-frequency radars, b) sea surface height, c) sea surface temperature, d) Corsica Channel mooring, e) in situ temperature, f) in situ salinity.

Time series of total northward transport through the CC for the three runs (FR, FC and AN) are shown in Figure 8a. The annual averages are 0.49, 0.31 and 0.28 Sv, respectively. These values are lower than previous estimates based on observations, ranging from 0.54 Sv to 0.71 Sv (Astraldi and Gasparini, 1992; Astraldi et al., 1994), and numerical models, such as 0.49 Sv in Sciascia et al. (2019) and 0.5 Sv in Béranger et al. (2005), the latter based on a multi-decadal time series. Part of the discrepancy with observational estimates may stem from the assumption of negligible longitudinal variability in the northward velocity across the channel that is not fully supported by our model results (Figure 6d, e) and was also observed by previous numerical studies Sciascia et al. (2019). However, some differences remain even when comparing our findings to other numerical studies. Additional analysis, particularly over a longer time period, will help determine whether the year 2022 reflects inter-annual variability (Vignudelli et al., 1999), or is the signal of a longer-term trend.

Both DA-informed simulations (FC and AN) show a net reduction in northward transport compared to the free run, although all three simulations capture expected seasonal variability, characterized by higher transport in winter and lower values in summer. The most notable differences occur in summer season and early fall: between June and October, average transport is 0.29 Sv in the FR and only 0.03 Sv in the AN. For the remaining part of the year, averages are 0.63 Sv and 0.45 Sv, respectively. Nonetheless, these results are not necessarily generalizable to other years, as DA could potentially increase transport in different conditions.

Figure 8b compares the increment in time-averaged transport estimated using the tangent linear approximation ($\Delta\overline{Tr}_{\mathrm{TL}}$, Equation 4) with that computed directly from the difference between the non-linear runs AN and FC ($\Delta\overline{Tr}_{\mathrm{NL}}$). The good

https://doi.org/10.5194/egusphere-2025-3806
Preprint. Discussion started: 15 August 2025

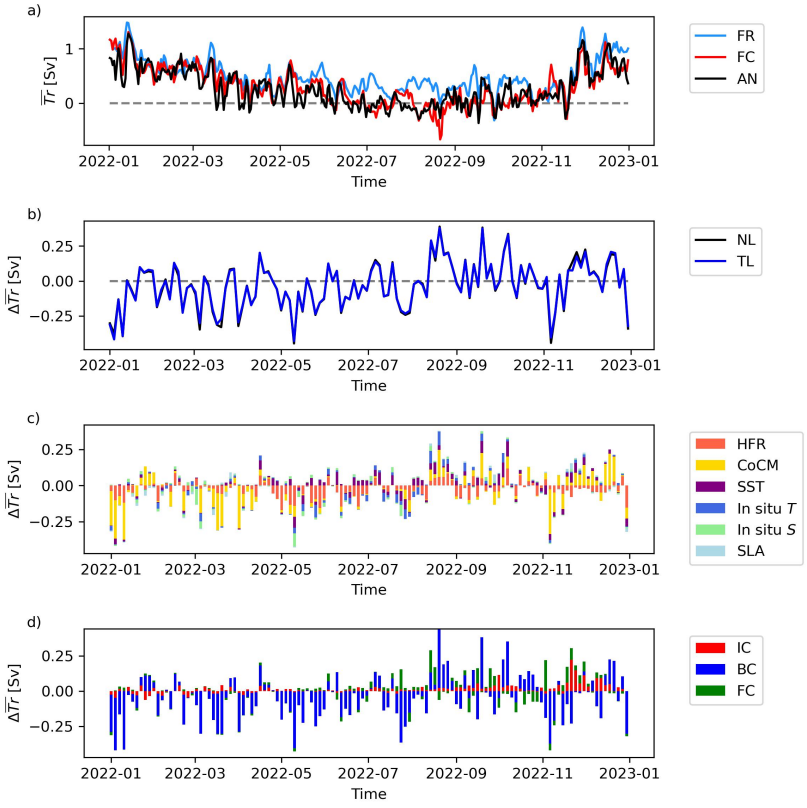

Figure 8. a) Total transport through the Corsica Channel for the freerun (light blue line), forecast (red line) and analysis (black line). b) Increment in total transport calculated by the difference between the analysis and background runs (black line) and through the tangent linear approximation (blue line). c) Impact of the different observation typologies in increasing/decreasing the total transport: HFR (orange bars), in situ CC mooring (yellow bars), SST (purple bars), in situ T (blue bars), in situ S (light green bars), SLA (light blue bars). d) Impact on increase/decrease of the total transport split by the correction applied to the background run: initial condition (IC, red bars), boundary conditions (BC, blue bars), atmospheric forcing (FC, green bars).

agreement between the two time series confirms that the tangent linear approximation holds well within the three-day assimilation window. Increments in average transport during an assimilation window range between -0.45 and 0.39 Sv, with a mean of -0.03 Sv and a standard deviation of 0.16 Sv.

The contribution of each observation type to changes in the total northward transport is shown in Figure 8c, as detailed in Section 2.3.

Observations from the CoCM have the largest overall impact on the transport increment, followed by HFR, SST, in situ T and S, and SLA. The relative impact of observation types also varies seasonally: CoCM data dominate during winter and autumn, while HFR observations have a greater influence during spring and summer. No clear seasonal pattern is observed for the remaining data sources.

https://doi.org/10.5194/egusphere-2025-3806
Preprint. Discussion started: 15 August 2025

Variable	RMS Impact [Sv]		
	Global $\cdot 10^{-2}$	**Datum** $\cdot 10^{-5}$	$\boldsymbol{N_{\text{obs}}} \cdot 10^{3}$
HFR	6.19	2.02	2194.8
CoCM	9.03	14.80	183.7
In situ T	2.64	5.45	625.2
In situ S	1.99	9.58	376.2
SST	3.63	1.68	1037.9
SLA	1.07	1.52	111.2

Table 2. Root mean square impact for the different observation typologies, both globally and considering the average contribution of a single observation. Last column reports the total number of observation per type.

An additional metric for evaluating observation impacts is the root mean square (RMS) of transport increments, calculated for both the aggregate effect of each observation type and for the average contribution of a single observation (Levin et al., 2021). The total RMS is calculated as $\sqrt{\frac{1}{N_{\text{w}}}\sum_{i=1}^{N_{\text{w}}}\Delta\overline{Tr}_{\text{w}}^{2}}$, where N_{w} is the total number of observations of a given type within an assimilation window. The average RMS impact per individual observation type is given by $\sqrt{\frac{1}{N_{\text{obs}}}\sum_{i=1}^{N_{\text{obs}}}(d_i \cdot g_i)^2}$, where N_{obs} is the total number of observations of a given type. Results for both measures are reported in Table 2.

In situ velocity observations from the CoCM are the most influential in constraining the CC transport, especially when considering the average impact per observation. Aggregated over time, HFR data emerge as the second most effective data source. However, each HFR observation is approximately 3-5 times less impactful than in situ T and S measurements, and about 7 times less impactful than CoCM data. While SST observations have greater overall impact than SLA on aggregate, the impact of individual observations of each type is similar (Table 2) reflecting the different number of observations N_{obs}.

Comparing the non-assimilative (FR) and the assimilative (AN) runs in Figure 6, it is clear that DA systematically reduces the northward velocity to better match the observations, leading to a corresponding reduction in total transport (Figure 8a). Interestingly, the total transport is less affected than the velocity alone. Figures 6d and e show that while the northward flow weakens across most of the transect in AN compared to FR, particularly on the eastern side, a partial compensation occurs through a weaker (in absolute value) southward flow on the western flank.

These differences between FR and AN are the cumulative result of corrections applied to the background by DA over each assimilation window. Importantly, observation impacts are computed with respect to the increments between background and analysis runs, not between analysis and freerun. With this in mind, Figure 8b, indicates that DA systematically reduces the northward transport up to mid-August 2022, after which positive transport increments become more frequent than negative increments. This evolving pattern is further dissected in Figure 8c): from January to early April, CoCM data primarily drive the transport corrections; between April and early August, HFR data become more influential, despite not being directly located at the CC transect, where the transport is computed. Figures 9a and c show the average velocity increment δv during the periods dominated by the JERICO facilities, CoCM (2022-01-01 to 2022-04-09) and HFR data (2022-04-22 to 2022-08-11), respectively.

https://doi.org/10.5194/egusphere-2025-3806
Preprint. Discussion started: 15 August 2025

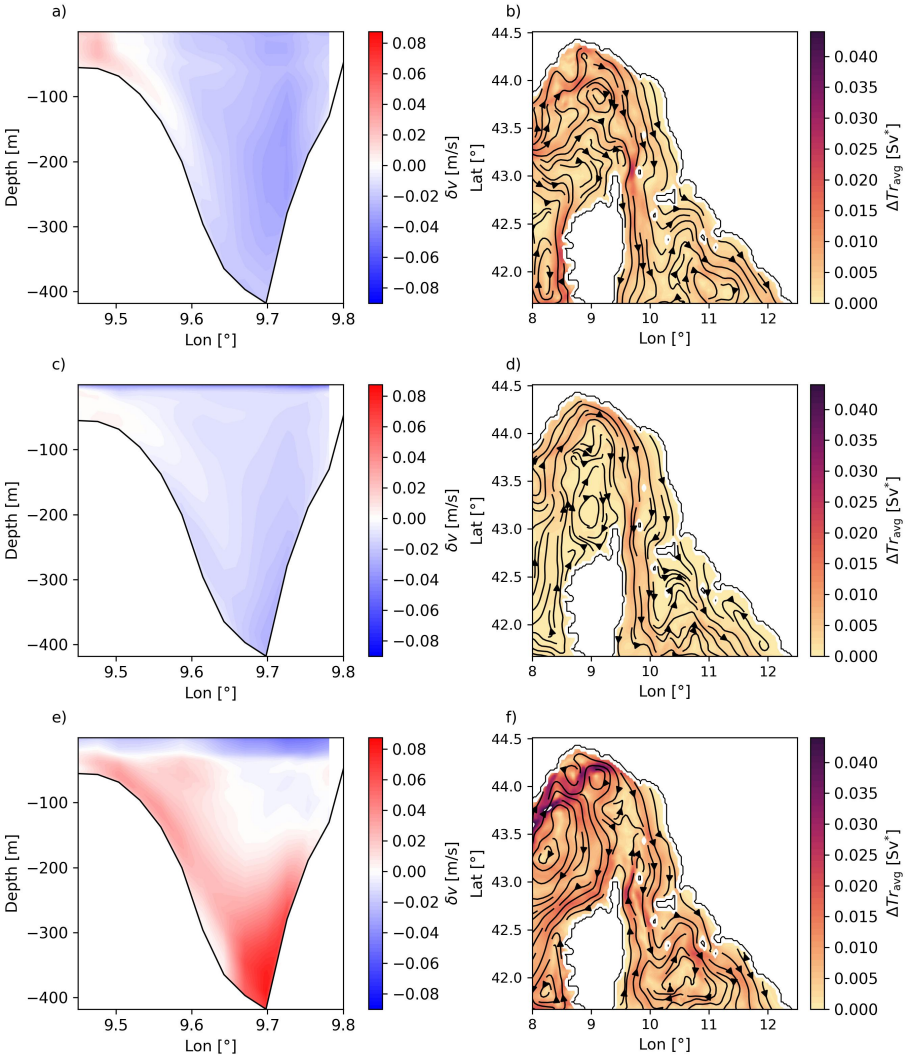

Figure 9. Time averaged values of the northward velocity increment δv at the Corsica Channel for specific time intervals: a) from 2022-01-01 to 2022-04-09; c) from 2022-04-22 to 2022-08-11; e) from 2022-11-18 to 2022-12-23. Time averaged values of the increment in transport magnitude ΔTr_{avg} for specific time intervals: b) from 2022-01-01 to 2022-04-09; d) from 2022-04-22 to 2022-08-11; f) from 2022-11-18 to 2022-12-23. Streamlines are created on the basis of the vector field ($\Delta Tr_{u,\text{avg}}$, $\Delta Tr_{v,\text{avg}}$). The measurement units is Sv* to indicate that the value is per cell of the domain.

https://doi.org/10.5194/egusphere-2025-3806
Preprint. Discussion started: 15 August 2025

CoCM observations tightly constrain the flow near their location but with the side effect of accelerating the northward flow in the surface western part of the transect. This could result from insufficient corrections to the boundary conditions, redirecting the volume transport to unconstrained portions of the domain (Figure 9a). Figure 9b shows the average spatial increment in transport per grid cell, defined as $\Delta Tr(x,y)_{\text{avg}} = \sqrt{\Delta Tr^2_{u,\text{avg}} + \Delta Tr^2_{v,\text{avg}}}$, where $\Delta Tr_{u,\text{avg}} = \frac{\Delta y}{T_\text{f}-T_\text{i}} \int_{T_\text{i}}^{T_\text{f}} \int_h \delta u \, dz \, dt$ and $\Delta Tr_{v,\text{avg}} = \frac{\Delta x}{T_\text{f}-T_\text{i}} \int_{T_\text{i}}^{T_\text{f}} \int_h \delta v \, dz \, dt$. Here Δx and Δy are cell dimensions, h is water depth, and T_i, T_f define the time interval (we prefer to consider this quantity rather than depth averaged velocity since the latter is independent of the volume of water moved). CoCM related transport increments show a pronounced southward pattern (Figure 9a and b), while HFR-driven increments manifest as surface- and bottom-intensified reductions in velocity, with weaker overall transport changes (Figure 9c and d). Furthermore, $\Delta Tr(x,y)_{\text{avg}}$ in Figure 9b is in general weaker than that of Figure 9d, despite the two show a similar pattern.

Another key period is from 2022-11-18 to 2022-12-23, when CoCM-driven positive increments are counterbalanced by HFR-driven reductions (Figure 8c). The corresponding average increment in velocity at the Corsica Channel cross section δv and the spatial distribution of $\Delta Tr(x,y)_{\text{avg}}$ for the eastern part of the modeled domain are reported in Figure 9e and f, respectively: it reveals surface deceleration from HFR and subsurface acceleration from CoCM. The corresponding average transport increment shows an east-west contrast, with acceleration near Capraia Island and deceleration across the Tuscany Archipelago (Figure 9f). This westward acceleration (at the eastern flank of Corsica) and eastward deceleration (at the Tuscany coast) is present at the southern boundary, where an anticyclonic structure in the average transport increment is formed.

Figure 8d quantifies the contribution of different components of the 4D-Var control vector (initial state, boundary conditions, surface fluxes of heat, freshwater and momentum) to the CC transport increment $\Delta\overline{Tr}$. The southern boundary corrections dominate throughout the year, indicating that transport is influenced by large-scale basin dynamics beyond the model's current spatial extent. Initial conditions have a limited role, except at the year's start and end, while surface forcing become more influential from June onward. This behaviour exemplifies a key feature of 4D-Var: the adjoint model $\mathbf{M}_\mathbf{b}^T$ uses the derivative $\partial I/\partial \mathbf{x}$ of the CC transport to inform the system that modifications are required at the boundaries to influence I during the 3 day assimilation window. For a more detailed explanation of the observation impact mechanism, see Levin et al. (2021). A more comprehensive analysis might expand the computational domain to the whole Western Mediterranean basin, though at significant computational costs.

Since $\Delta\overline{Tr}_{\text{TL}} = \mathbf{d}^T \cdot \mathbf{g}$, the spatial variation in the elements of $\mathbf{g}$ reveals which observations have the greatest influence on the model. Figure 10 shows the spatial distribution of the root mean squared values of the elements of $\mathbf{g}$ (RMSg) calculated over each computational cell for each observation type.

RMSg for HFR peaks near the eastern part of the coverage region and close to the coast (Figure 10a), aligning with the CC's longitudinal range ($9.45°\text{E} - 9.8°\text{E}$). The degree of sensitivity of the transport to SST data (Figure 10c) shows that observations located close to the CC, adjacent to the open boundary, and those surrounding the Rhone river outflow (4.848°E, 43.328°N) and the mouth of the Arno river (10.274°E, 43.680°N), potentially have a larger impact on transport than SST observations located elsewhere. High sensitivity near river mouths may be partly explained by the background-error covariance matrix $\mathbf{B}$ that we assumed proportional to the standard deviation of the freerun. However, looking at the upper layer of the temperature standard deviation (not shown), larger values are present only at the Rhone river mouth, meaning that the sensitivity of the

https://doi.org/10.5194/egusphere-2025-3806
Preprint. Discussion started: 15 August 2025

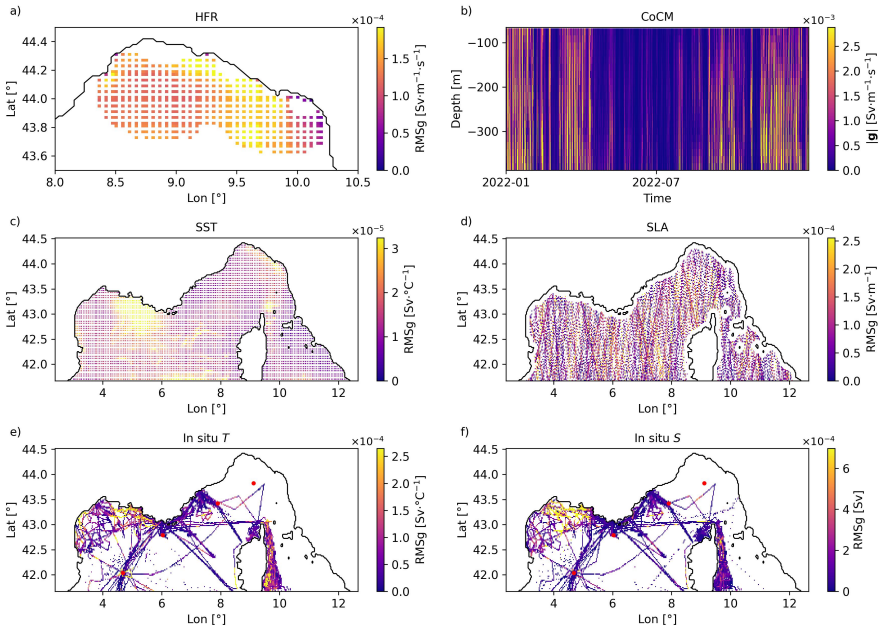

Figure 10. Spatial distribution of the root mean squared values of $\mathbf{g}$ (RMSg), for different observations: HFR a), SST c), SLA d), in situ T e), in situ S f). b) Absolute value of $\mathbf{g}$ as a function of observation depth and time for the v-velocity measured by the CoCM. Red dots represent the locations of the EMSO stations (see Figure 1a for the abbreviations associated to each station).

transport through the CC, to the other areas with high RMSg, is induced by the adjoint model. Furthermore, large $\mathbf{B}$ values are not sufficient alone to explain high RMSg, meaning that even the circulation at Rhone river mouth can influence the CC transport. The impact of SLA observations shows no clear spatial pattern (Figure 10d), although certain satellite tracks exhibit a larger RMSg values, suggesting that during specific periods the barotropic control on CC transport is significant. Indeed, if we plot the g_i values as a function of time (not shown), we observe larger values at the year's start and end, suggesting that when Tr_{CC} is higher, corrections of the barotropic modes are larger. In situ T and S sensitivity (Figures 10e and f) is highest near the Rhone river and the Gulf of Lion, with secondary hotspots near the LI station and around the southern area of Corsica, especially for T. These results emphasize that distant observations can significantly affect CC transport.

Figure 10b shows a Hovmöeller diagram of the absolute values of the elements of $\mathbf{g}$ associated with the v-velocity component of the velocity observations from the CoCM. The sensitivity of Tr_{CC} to these v-velocity observations appears relatively uniform with depth and displays a clear seasonal signal, consistent with the temporal variability seen in Figure 8d, where the contribution of CoCM data diminishes during late spring and summer. Although the vertical distribution of sensitivity is generally homogeneous, it tends to be more pronounced at the bottom. This may result from the fact that the $\mathbf{g}$ values are weighted by the $\mathbf{P}$ matrix (through the Kalman gain, see Equation 3), thus depending on $\mathbf{R}$, $\mathbf{B}$, and the spatial distribution of the other observations. As a result, the sensitivity of Tr_{CC} to CoCM data near the surface may be partially influenced by HFR, SST, SLA observations whereas at depth this effect is not present.

https://doi.org/10.5194/egusphere-2025-3806
Preprint. Discussion started: 15 August 2025

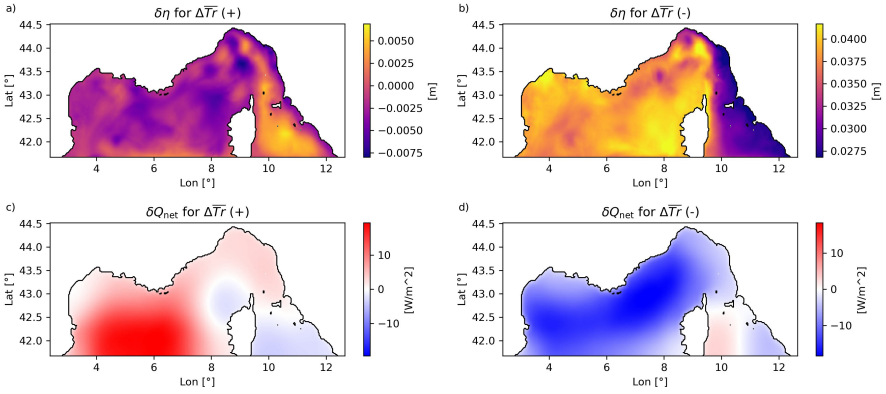

Figure 11. Time averaged difference between analysis and Background over specific assimilation windows for the fields free surface η and net heat flux Q_{net} in case the increment in transport $\Delta\overline{Tr}$ is positive, a), c), and in case it is negative b), d).

Focusing on the g_i values helps to identify observation locations that are potentially influential for $\Delta\overline{Tr}$ and, by extension, for understanding the physical mechanisms driving transport in the CC. In contrast, analyzing the product $d_i \cdot g_i$ (i.e., individual increments) may mask this insight, as a large sensitivity g_i could be masked by a small innovation d_i, or vice versa. A more targeted approach to quantify the influence of different regions or variables on the CC transport would be an adjoint sensitivity study (Moore et al., 2009; Veneziani et al., 2009). However, such an approach does not offer information about how observational data significantly shape the model solution.

Astraldi and Gasparini (1992) proposed that CC dynamics are governed by atmospheric conditions over the western part of the Ligurian-Provençal basin, where winter heat loss enhances the steric gradient between the Tyrrhenian and Ligurian-Provençal basins, driving Tyrrhenian waters into the Ligurian Sea and strengthening the ECC. Our results reveal two related but distinct DA-driven mechanisms. By selecting assimilation windows with the largest positive and negative transport increments (90-th and 10-th percentiles of the ΔTr distribution, respectively), we calculated the free surface height change $\delta\eta$ (Figure 11a and b) and net heat flux δQ_{net} (Figure 11c and d) between analysis and background states, averaged over the two sets of assimilation windows. These transport increments are for the most part induced by changes of the boundary conditions (Figure 8d). A positive δTr is indeed associated with a northward-inducing $\delta\eta$ (Figure 11a), but also with a positive Q_{net}. To adjust to $\delta\eta$, the density in the western part must increase and that on the Tyrrhenian side decrease (or increase to a lesser extent) through differential cooling of the water body. We argue that, in order to maintain consistency with the observations, this cooling is counteracted by a positive δQ_{net} (Figure 11c). A decrease in transport is associated with a more pronounced gradient in $\delta\eta$, which remains positive all over the domain, as shown in Figure 11b (see colorbar). Again, to compensate for the density decrease driven by $\delta\eta$, the DA system tends to cool the western side more via a pronounced negative δQ_{net}. This behavior contrasts with the mechanism described by Astraldi and Gasparini (1992), where heat loss is the driver of the ECC acceleration, whereas, in our case, heat supply is a consequence of the mechanism employed by the DA procedure to constrain the model toward observations when ECC accelerates (anc vice-versa).

https://doi.org/10.5194/egusphere-2025-3806
Preprint. Discussion started: 15 August 2025

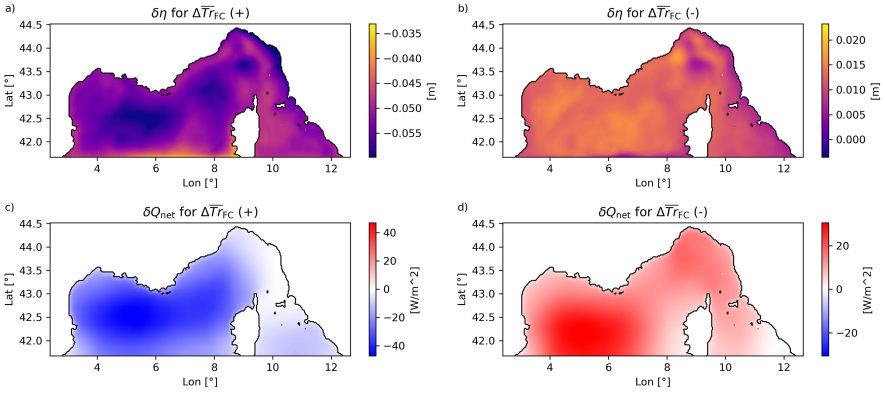

Figure 12. Time averaged difference between analysis and Background over specific assimilation windows for the fields net heat flux Q_{net}, net fresh water flux F_{net}, and wind stress curl τ_{w}, in case the increment in transport only due to adjustments to the atmospheric forcing $\Delta\overline{Tr}_{\text{FC}}$ is positive, a), c), e), and in case it is negative b), d), f).

Focusing now on the largest positive and negative transport increments attributable solely to the correction to atmospheric forcing, $\Delta\overline{Tr}_{\text{FC}}$, we observe in Figure 12c and d that δQ_{net} aligns with the mechanism proposed by Astraldi and Gasparini (1992): an increase (decrease) in transport is triggered by a differential surface cooling (warming), despite the $\delta\eta$ pattern is less pronounced (Figure 12a and b) than that induced by modifications to the boundary conditions (Figure 11a and b). Indeed, unlike the case in which boundary conditions drive $\Delta\overline{Tr}$, here it is the adjustment in heat flux that initiates the response. For the increments in net freshwater flux and the wind stress curl, we did not observe patterns which can play specific role in driving the changes in $\Delta\overline{Tr}_{\text{FC}}$. Both mechanisms show that the geostrophic balance plays a fundamental role in shaping the dynamics of the CC.

4 Conclusions

The ECC is a key feature of the north-western Mediterranean Sea circulation, transporting Tyrrhenian waters into the Ligurian Sea. In this study, we used the ROMS 4D-Var system to assess how various observations constrain the transport through the CC and to investigate the mechanisms underlying its variability. Surface velocities from HFR, SST, SLA, in situ temperature, salinity and velocity profiles-measured directly in the CC were assimilated for the year 2022 using 3 days assimilation windows, with one outer loop and nine inner loops.

The results from the analysis (AN) and forecast (FC) runs show significant improvements in the representation of circulation, compared to the free run (FR) without data assimilation. RMSE reductions ranged from 8.3% to 34.1% in the FC and from 18.7% to 62.4% in the AN. Pearson correlation coefficients (ρ) increased by 0.04 to 0.31 in the FC and by 0.04 to 0.41 in the AN. While BIAS values in the forecast exhibited both increases and decreases, reductions were dominant in the analysis.

https://doi.org/10.5194/egusphere-2025-3806
Preprint. Discussion started: 15 August 2025

After assimilation, the annual mean transport through the CC decreased from 0.49 Sv in the FR to 0.31 Sv in the FC and 0.28 Sv in the AN. The comparison between the AN and FR indicates that the ECC deceleration is accompanied by an acceleration of the WCC, occurring both at the surface (AW) and at intermediate depths (EIW).

The reduction in CC transport is mainly attributed to the assimilation of CoCM data, which generally slow down the ECC during the first part of the year, and then contribute to its acceleration from September onward. HFR data represent the second most influential source for constraining CC transport, particularly contributing to the reduction during late spring and summer. SST, in situ temperature and salinity, and SLA follow in importance. The various data types influence the northward velocity pattern across the CC differently, sometimes competing, as in the case where HFR data tend to decelerate surface flow, while CoCM data can accelerate flow at depth. Transport sensitivity analyses reveal that circulation features located far from the CC, such as those in the Gulf of Lion, can also significantly influence the flow.

The analysis of the control vector elements shows that corrections to open boundary conditions have the largest impact on transport changes, followed by initial conditions and atmospheric forcing. During periods of major ECC modifications, these adjustments work continuously across the DA window to generate free surface gradients in the state increment, which can increase or decrease CC transport. Meanwhile, DA ensures the consistency of the model with observations throughout the domain.

Corrections to atmospheric forcing behaves differently in case they are a consequence of the adjustment to the model state (when boundary conditions control the increment), or when they act as the main driver of it.

Future work will extend the analysis both backward and forward in time to evaluate the impact of assimilated observations on the interannual variability of CC transport. Additionally, further attention will be dedicated to investigating the dynamics of the WCC and its role in the broader regional circulation.

Author contributions. **M.B.**: conceptualization, formal analysis, investigation, methodology, software, supervision, validation, visualization, writing – original draft, writing – review and editing. **A.M.M.**: conceptualization, methodology, writing – review and editing. **R.S.**: conceptualization, writing – review and editing. **C.B.**: conceptualization, resources. **K.S.**: data curation, funding acquisition, writing – review and editing. **M.B.**: data curation, funding acquisition. **M.G.M.**: conceptualization, data curation, funding acquisition, resources, writing – review and editing.

Competing interests. The authors declare that they have no conflict of interest.

Acknowledgements. This research was funded by the European Union—NextGenerationEU and the Ministry of University and Research (MUR), National Recovery and Resilience Plan (NRRP), Mission 4, Component 2, Investment 1.5, project "RAISE—Robotics and AI for Socio-economic Empowerment" (ECS00000035). **M.B.** was fully supported by the the European Union—NextGenerationEU and the Ministry of University and Research (MUR), National Recovery and Resilience Plan (NRRP), Mission 4, Component 2, Investment 1.5,

https://doi.org/10.5194/egusphere-2025-3806
Preprint. Discussion started: 15 August 2025

project “RAISE—Robotics and AI for Socio-economic Empowerment” (ECS00000035) project. **R.S.** and **M.G.M.** were partially supported by the EU - Next Generation Mission 4, Component 2 - CUP B53C22002150006 - IR0000032 – ITINERIS (Italian Integrated Environmental Research Infrastructures System) Project. The authors acknowledge partial support from the European project JERICO-S3 (H2020 grant agreement No 871153) for the data collection at the Corsica Channel mooring site.

https://doi.org/10.5194/egusphere-2025-3806
Preprint. Discussion started: 15 August 2025

References

Aracri, S., Borghini, M., Canesso, D., Chiggiato, J., Durante, S., Schroeder, K., Sparnocchia, S., Vetrano, A., Honda, T., Kitawaza, Y., et al.: Trials of an autonomous profiling buoy system, Journal of Operational Oceanography, 9, s176–s184, 2016.

Arango, H. G., Levin, J. C., Curchitser, E. N., Zhang, B., Moore, A. M., Han, W., Gordon, A. L., Lee, C. M., and Girton, J. B.: Development of a hindcast/forecast model for the Philippine Archipelago, Oceanography, 24, 58–69, 2011.

Artale, V. and Gasparini, G.: Simultaneous temperature and velocity measurements of the internal wave field in the Corsican Channel (Eastern Ligurian Sea), Journal of Geophysical Research: Oceans, 95, 1635–1645, 1990.

Astraldi, M. and Gasparini, G.: The seasonal characteristics of the circulation in the north Mediterranean basin and their relationship with the atmospheric-climatic conditions, Journal of Geophysical Research: Oceans, 97, 9531–9540, 1992.

Astraldi, M., Gasparini, G., Manzella, G., and Hopkins, T.: Temporal variability of currents in the eastern Ligurian Sea, Journal of Geophysical Research: Oceans, 95, 1515–1522, 1990.

Astraldi, M., Gasparini, G. P., and Sparnocchia, S.: The seasonal and interannual variability in the Ligurian-Provençal basin, Seasonal and interannual variability of the Western Mediterranean Sea, 46, 93–113, 1994.

Astraldi, M., Bianchi, C. N., Gasparini, G. P., and Morri, C.: Climatic fluctuations, current variability and marine species distribution: a case study in the Ligurian Sea (North-West Mediterranean), Oceanologica Acta, 18, 139–149, 1995.

Aydogdu, A., Escudier, R., Hernandez-Lasheras, J., Amadio, C., Pistoia, J., Zarokanellos, N. D., Cossarini, G., Remy, E., and Mourre, B.: Glider observations in the Western Mediterranean Sea: their assimilation and impact assessment using four analysis and forecasting systems, Frontiers in Marine Science, 12, 1456 463, 2025.

Bajo, M., Ferrarin, C., Umgiesser, G., Bonometto, A., and Coraci, E.: Modelling the barotropic sea level in the Mediterranean Sea using data assimilation, Ocean Science, 19, 559–579, 2023.

Bendoni, M., Moore, A. M., Molcard, A., Magaldi, M. G., Fattorini, M., and Brandini, C.: 4D-Var data assimilation and observation impact on surface transport of HF-Radar derived surface currents in the North-Western Mediterranean Sea, Ocean Modelling, 184, 102 236, 2023.

Béranger, K., Mortier, L., and Crépon, M.: Seasonal variability of water transport through the Straits of Gibraltar, Sicily and Corsica, derived from a high-resolution model of the Mediterranean circulation, Progress in Oceanography, 66, 341–364, 2005.

Bethoux, J.: Mean water fluxes across sections in the Mediterranean-Sea, evaluated on the basis of water and salt budgets and of observed salinities, Oceanologica Acta, 3, 79–88, 1980.

Buongiorno-Nardelli, B., Tronconi, C., Pisano, A., and Santoleri, R.: High and Ultra-High resolution processing of satellite Sea Surface Temperature data over Southern European Seas in the framework of MyOcean project, Remote Sensing of Environment, 129, 1–16, 2013.

Chapman, D. C.: Numerical treatment of cross-shelf open boundaries in a barotropic coastal ocean model, Journal of Physical oceanography, 15, 1060–1075, 1985.

Ciuffardi, T., Napolitano, E., Iacono, R., Reseghetti, F., Raiteri, G., and Bordone, A.: Analysis of surface circulation structures along a frequently repeated XBT transect crossing the Ligurian and Tyrrhenian Seas, Ocean Dynamics, 66, 767–783, 2016.

Coppola, L., Diamond Riquier, E., and Carval, T.: Dyfamed observatory data, 2019.

Courtier, P., Thépaut, J.-N., and Hollingsworth, A.: A strategy for operational implementation of 4D-Var, using an incremental approach, Quarterly Journal of the Royal Meteorological Society, 120, 1367–1387, 1994.

https://doi.org/10.5194/egusphere-2025-3806
Preprint. Discussion started: 15 August 2025

Dobricic, S., Pinardi, N., Adani, M., Bonazzi, A., Fratianni, C., and Tonani, M.: Mediterranean Forecasting System: An improved assimilation scheme for sea-level anomaly and its validation, Quarterly Journal of the Royal Meteorological Society: A journal of the atmospheric sciences, applied meteorology and physical oceanography, 131, 3627–3642, 2005.

Escudier, R., Clementi, E., Cipollone, A., Pistoia, J., Drudi, M., Grandi, A., Lyubartsev, V., Lecci, R., Aydogdu, A., Delrosso, D., et al.: A high resolution reanalysis for the Mediterranean Sea, Frontiers in Earth Science, 9, 702 285, 2021.

Fairall, C. W., Bradley, E. F., Rogers, D. P., Edson, J. B., and Young, G. S.: Bulk parameterization of air-sea fluxes for tropical ocean-global atmosphere coupled-ocean atmosphere response experiment, Journal of Geophysical Research: Oceans, 101, 3747–3764, 1996.

Fang, Y.-C., Weingartner, T. J., Potter, R. A., Winsor, P. R., and Statscewich, H.: Quality Assessment of HF Radar–Derived Surface Currents Using Optimal Interpolation, Journal of Atmospheric and Oceanic Technology, 32, 282–296, 2015.

Flather, R.: A tidal model of the north-west European continental shelf, Memoires de la Societe Royale de Sciences de Liege, 6, 141–164, 1976.

Fossi, M. C., Romeo, T., Panti, M., Marsili, L., Campani, T., Canese, S., Galgani, F., Druon, J., Airoldi, S., Taddei, S., Fattorini, M., Brandini, C., and Lapucci, C.: Plastic debris occurrence, convergence areas and fin whales feeding ground in the Mediterranean Marine Protected Area Pelagos Sanctuary: a modeling approach, Frontiers in Marine Science, 4, 167, 2017.

Francour, P., Harmelin, J.-G., Pollard, D., and Sartoretto, S.: A review of marine protected areas in the northwestern Mediterranean region: siting, usage, zonation and management, Aquatic conservation: marine and freshwater ecosystems, 11, 155–188, 2001.

Fujii, Y., Yoshida, T., Sugimoto, H., Ishikawa, I., and Urakawa, S.: Evaluation of a global ocean reanalysis generated by a global ocean data assimilation system based on a four-dimensional variational (4DVAR) method, Frontiers in Climate, 4, 1019 673, 2023.

Gürol, S., Weaver, A. T., Moore, A. M., Piacentini, A., Arango, H. G., and Gratton, S.: B-preconditioned minimization algorithms for variational data assimilation with the dual formulation, Quarterly Journal of the Royal Meteorological Society, 140, 539–556, 2014.

Hernandez-Lasheras, J. and Mourre, B.: Dense CTD survey versus glider fleet sampling: comparing data assimilation performance in a regional ocean model west of Sardinia, Ocean Science, 14, 1069–1084, 2018.

Hernandez-Lasheras, J., Mourre, B., Orfila, A., Santana, A., Reyes, E., and Tintoré, J.: Evaluating high-frequency radar data assimilation impact in coastal ocean operational modelling, Ocean Science, 17, 1157–1175, 2021.

Hersbach, H., Bell, B., Berrisford, P., Biavati, G., Horányi, A., Muñoz Sabater, J., Nicolas, J., Peubey, C., Radu, R., Rozum, I., et al.: ERA5 hourly data on single levels from 1940 to present, Copernicus Climate Change Service (C3S) Climate Data Store (CDS)[data set], 2023.

Houpert, L., Durrieu de Madron, X., Testor, P., Bosse, A., d'Ortenzio, F., Bouin, M.-N., Dausse, D., Le Goff, H., Kunesch, S., Labaste, M., et al.: Observations of open-ocean deep convection in the northwestern M editerranean S ea: Seasonal and interannual variability of mixing and deep water masses for the 2007-2013 Period, Journal of Geophysical Research: Oceans, 121, 8139–8171, 2016.

Iermano, I., Moore, A., and Zambianchi, E.: Impacts of a 4-dimensional variational data assimilation in a coastal ocean model of southern Tyrrhenian Sea, Journal of Marine Systems, 154, 157–171, 2016.

Janeković, I., Powell, B., Matthews, D., McManus, M., and Sevadjian, J.: 4D-Var data assimilation in a nested, coastal ocean model: A Hawaiian case study, Journal of Geophysical Research: Oceans, 118, 5022–5035, 2013.

Janeković, I., Mihanović, H., Vilibić, I., Grčić, B., Ivatek-Šahdan, S., Tudor, M., and Djakovac, T.: Using multi-platform 4D-Var data assimilation to improve modeling of Adriatic Sea dynamics, Ocean Modelling, 146, 101 538, 2020.

Janeković, I., Rayson, M., Jones, N., Watson, P., and Pattiaratchi, C.: 4D-Var data assimilation using satellite sea surface temperature to improve the tidally-driven interior ocean dynamics estimates in the Indo-Australian Basin, Ocean Modelling, 171, 101 969, 2022.

https://doi.org/10.5194/egusphere-2025-3806
Preprint. Discussion started: 15 August 2025

Kerry, C., Roughan, M., and Powell, B.: Predicting the submesoscale circulation inshore of the East Australian Current, Journal of Marine Systems, 204, 103 286, 2020.

Langland, R. H. and Baker, N. L.: Estimation of observation impact using the NRL atmospheric variational data assimilation adjoint system, Tellus A: Dynamic Meteorology and Oceanography, 56, 189–201, 2004.

Lefevre, D., Tamburini, C., Bhairy, N., Chirurgien, L., Gojak, C., Bernardet, K., Hafidi, Z., and Mahiouz, K.: EMSO-Ligure Ouest observatory data (mooring ALBATROSS), 2016.

Levin, J., Arango, H. G., Laughlin, B., Hunter, E., Wilkin, J., and Moore, A. M.: Observation impacts on the Mid-Atlantic Bight front and cross-shelf transport in 4D-Var ocean state estimates: Part I—Multiplatform analysis, Ocean Modelling, 156, 101 721, 2020.

Levin, J., Arango, H. G., Laughlin, B., Wilkin, J., and Moore, A. M.: The impact of remote sensing observations on cross-shelf transport estimates from 4D-Var analyses of the Mid-Atlantic Bight, Advances in space research, 68, 553–570, 2021.

Marchesiello, P., McWilliams, J. C., and Shchepetkin, A.: Open boundary conditions for long-term integration of regional oceanic models, Ocean modelling, 3, 1–20, 2001.

Marmain, J., Molcard, A., Forget, P., Barth, A., and Ourmieres, Y.: Assimilation of HF radar surface currents to optimize forcing in the northwestern Mediterranean Sea, Nonlinear Processes in Geophysics, 21, 659–675, 2014.

McIntosh, P. and Bennett, A.: Open ocean modeling as an inverse problem: M 2 tides in Bass Strait, Journal of Physical Oceanography, 14, 601–614, 1984.

Millot, C.: Circulation in the western Mediterranean Sea, Journal of Marine Systems, 20, 423–442, 1999.

Moore, A. M., Arango, H. G., Di Lorenzo, E., Miller, A. J., and Cornuelle, B. D.: An adjoint sensitivity analysis of the Southern California Current circulation and ecosystem, Journal of Physical Oceanography, 39, 702–720, 2009.

Moore, A. M., Arango, H. G., Broquet, G., Edwards, C., Veneziani, M., Powell, B., Foley, D., Doyle, J. D., Costa, D., and Robinson, P.: The Regional Ocean Modeling System (ROMS) 4-dimensional variational data assimilation systems: Part III–Observation impact and observation sensitivity in the California Current System, Progress in Oceanography, 91, 74–94, 2011a.

Moore, A. M., Arango, H. G., Broquet, G., Powell, B. S., Weaver, A. T., and Zavala-Garay, J.: The Regional Ocean Modeling System (ROMS) 4-dimensional variational data assimilation systems: Part I–System overview and formulation, Progress in Oceanography, 91, 34–49, 2011b.

Moore, A. M., Edwards, C. A., Fiechter, J., Drake, P., Neveu, E., Arango, H. G., Gürol, S., and Weaver, A. T.: A 4D-Var analysis system for the California Current: A prototype for an operational regional ocean data assimilation system, in: Data Assimilation for Atmospheric, Oceanic and Hydrologic Applications (Vol. II), pp. 345–366, Springer, 2013.

Moore, A. M., Jacox, M. G., Crawford, W. J., Laughlin, B., Edwards, C. A., and Fiechter, J.: The impact of the ocean observing system on estimates of the California current circulation spanning three decades, Progress in Oceanography, 156, 41–60, 2017.

Moore, A. M., Arango, H. G., and Edwards, C. A.: Reduced-rank array modes of the California current observing system, Journal of Geophysical Research: Oceans, 123, 452–465, 2018.

Moore, A. M., Levin, J., Arango, H. G., and Wilkin, J.: Assessing the performance of an ocean observing, analysis and forecast System for the Mid-Atlantic Bight using array modes, Ocean Modelling, 164, 101 821, 2021.

Notarbartolo-di Sciara, G., Agardy, T., Hyrenbach, D., Scovazzi, T., and Van Klaveren, P.: The Pelagos sanctuary for Mediterranean marine mammals, Aquatic Conservation: Marine and Freshwater Ecosystems, 18, 367–391, 2008.

Poulain, P.-M., Mauri, E., Gerin, R., Chiggiato, J., Schroeder, K., Griffa, A., Borghini, M., Zambianchi, E., Falco, P., Testor, P., et al.: On the dynamics in the southeastern Ligurian Sea in summer 2010, Continental Shelf Research, 196, 104 083, 2020.

https://doi.org/10.5194/egusphere-2025-3806
Preprint. Discussion started: 15 August 2025

Schroeder, K., Josey, S. A., Herrmann, M., Grignon, L., Gasparini, G. P., and Bryden, H. L.: Abrupt warming and salting of the Western Mediterranean Deep Water after 2005: Atmospheric forcings and lateral advection, Journal of Geophysical Research: Oceans, 115, C08 029, 2010.

Schroeder, K., Ismail, S. B., Manuel, B., Anthony, B., Jacopo, C., Giuseppe, C., Giannetta, F., Miroslav, G., Isaac, G., Elisabeth, K., et al.: A consensus-based, revised and comprehensive catalogue for Mediterranean water masses acronyms, Mediterranean Marine Science, 25, 783–791, 2024.

Sciascia, R., Magaldi, M. G., and Vetrano, A.: Current reversal and associated variability within the Corsica Channel: The 2004 case study, Deep Sea Research Part I: Oceanographic Research Papers, 144, 39–51, 2019.

Shchepetkin, A. F. and McWilliams, J. C.: A method for computing horizontal pressure-gradient force in an oceanic model with a nonaligned vertical coordinate, Journal of Geophysical Research: Oceans, 108, 2003.

Shchepetkin, A. F. and McWilliams, J. C.: The regional oceanic modeling system (ROMS): a split-explicit, free-surface, topography-following-coordinate oceanic model, Ocean modelling, 9, 347–404, 2005.

Sperrevik, A. K., Christensen, K. H., and Röhrs, J.: Constraining energetic slope currents through assimilation of high-frequency radar observations, Ocean Science, 11, 237–249, 2015.

Szekely, T., Gourrion, J., Pouliquen, S., Reverdin, G., and Merceur, F.: CORA, coriolis ocean dataset for reanalysis. SEANOE, 2025.

Tac, C. M. I. S.: Copernicus Marine In Situ TAC NetCDF format manual, 2023.

Teruzzi, A., Bolzon, G., Salon, S., Lazzari, P., Solidoro, C., and Cossarini, G.: Assimilation of coastal and open sea biogeochemical data to improve phytoplankton simulation in the Mediterranean Sea, Ocean Modelling, 132, 46–60, 2018.

Vandenbulcke, L., Beckers, J.-M., and Barth, A.: Correction of inertial oscillations by assimilation of HF radar data in a model of the Ligurian Sea, Ocean Dynamics, 67, 117–135, 2017.

Veneziani, M., Edwards, C., and Moore, A.: A central California coastal ocean modeling study: 2. Adjoint sensitivities to local and remote forcing mechanisms, Journal of Geophysical Research: Oceans, 114, 2009.

Vignudelli, S., Gasparini, G., Astraldi, M., and Schiano, M.: A possible influence of the North Atlantic Oscillation on the circulation of the Western Mediterranean Sea, Geophysical Research Letters, 26, 623–626, 1999.

Warner, J. C., Sherwood, C. R., Arango, H. G., and Signell, R. P.: Performance of four turbulence closure models implemented using a generic length scale method, Ocean Modelling, 8, 81–113, 2005.

Weaver, A. and Courtier, P.: Correlation modelling on the sphere using a generalized diffusion equation, Quarterly Journal of the Royal Meteorological Society, 127, 1815–1846, 2001.

Zavala-Garay, J., Wilkin, J., and Arango, H.: Predictability of mesoscale variability in the East Australian Current given strong-constraint data assimilation, Journal of physical oceanography, 42, 1402–1420, 2012.

Zavala-Garay, J., Wilkin, J., and Levin, J.: Data assimilation in coastal oceanography: IS4DVAR in the Regional Ocean Modelling System (ROMS), in: Advanced Data Assimilation for Geosciences: Lecture Notes of the Les Houches School of Physics: Special Issue, June 2012, Oxford University Press, ISBN 9780198723844, 2014.

Zhang, W. G., Wilkin, J. L., and Arango, H. G.: Towards an integrated observation and modeling system in the New York Bight using variational methods. Part I: 4DVAR data assimilation, Ocean Modelling, 35, 119–133, 2010.